ACS OMEGA

Open Access



http://pubs.acs.org/journal/acsodf

Article

# Machine Learning Enabled Multidimensional Data Utilization Through Multi-Resonance Architecture: A Pathway to Enhanced Accuracy in Biosensing

Majid Aalizadeh, Morteza Azmoudeh Afshar, and Xudong Fan*

Cite This: *ACS Omega* 2025, 10, 20713−20722

Read Online

ACCESS | Metrics & More | Article Recommendations | Supporting Information

**ABSTRACT:** A novel framework is proposed that combines multiresonance biosensors with machine learning (ML) to significantly enhance the accuracy of parameter prediction in biosensing. Unlike traditional single-resonance systems, which are limited to one-dimensional data sets, this approach leverages multidimensional data generated by a custom-designed nanostructure—a periodic array of silicon nanorods with a triangular cross section over an aluminum reflector. High bulk sensitivity values are achieved for this multiresonant structure, with certain resonant peaks reaching up to 1706 nm/RIU. The field analysis reveals Mie resonances as the physical reason behind the peaks. The predictive power of multiple resonant peaks from transverse magnetic and transverse electric polarizations is evaluated using Ridge Regression modeling. Systematic analysis reveals that incorporating multiple resonances yields up to 3 orders of magnitude improvement in refractive index detection precision compared to single-peak analyses. This precision enhancement is achieved without modifications to the biosensor hardware, highlighting the potential of data-centric strategies in biosensing. The findings establish a new paradigm in biosensing, demonstrating that the synergy between multiresonance data acquisition and ML-based analysis can significantly enhance detection accuracy. This study provides a scalable pathway for advancing high-precision biosensing technologies.

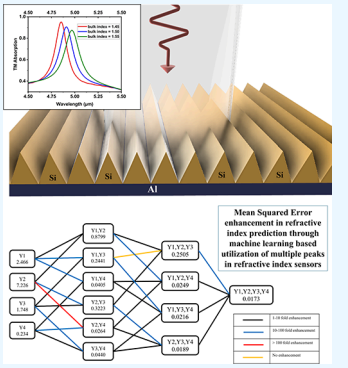


**KEYWORDS:** *Machine learning, Multi-resonance, index sensor, multi-dimensional data, ridge regression*



## 1. INTRODUCTION

A notable innovation in optical biosensing is the use of resonant structures that enhance detection performance through light-nanostructure interactions.[1−9] Traditionally, single-resonance biosensors offer a single measurable response to external changes like refractive index variations.[10−16] Refractive index sensors are used in biosensing and medical diagnostics, chemical and environmental sensing, food and beverage quality control, optical and photonic devices, pharmaceutical analysis, industrial monitoring.[17−24] Index However, the limitations of single-resonance systems[25,26] in capturing complex, multidimensional biological signals have led to the exploration of new approaches. Introducing multiresonant structures[27−31] presents a transformative advancement in the field, enabling the collection of richer, multidimensional data sets and paving the way for improved precision and robustness in parameter prediction.

Machine learning (ML) has become a groundbreaking tool in biosensing, facilitating the analysis and interpretation of complex, high-dimensional data.[32−36] Combining multiresonance biosensors with ML methods can significantly enhance the precision of target variable predictions. This combination is particularly effective with multidimensional data sets that contain latent correlations and patterns not evident in lower-dimensional data. Traditional one-dimensional (1D) biosensing data have often been modeled using simple linear fittings, which may not provide optimal precision.[37,38]

Here, we propose a novel framework to overcome these limitations by utilizing multidimensional data and demonstrate the high potential of utilizing multidimensional data in biosensing through an exemplary optical multiresonant structure. Our approach is based on the principle that incorporating multiple predictors or resonances leads to superior prediction accuracy of the target variable compared to using lower-dimensional or 1D data. This hypothesis is validated by modeling a relatively simple-to-fabricate nanostructure consisting of a triangular cross-sectioned array of periodic silicon nanorods over an aluminum back reflector.

Most resonant peaks in our structure exhibit sensitivity values in the hundreds of nm/RIU, with specific peaks reaching bulk sensitivity as high as 1706 nm/RIU. It is shown through electric and magnetic field analysis that the magnetic

**Received:** February 23, 2025
**Revised:** April 6, 2025
**Accepted:** May 8, 2025
**Published:** May 15, 2025

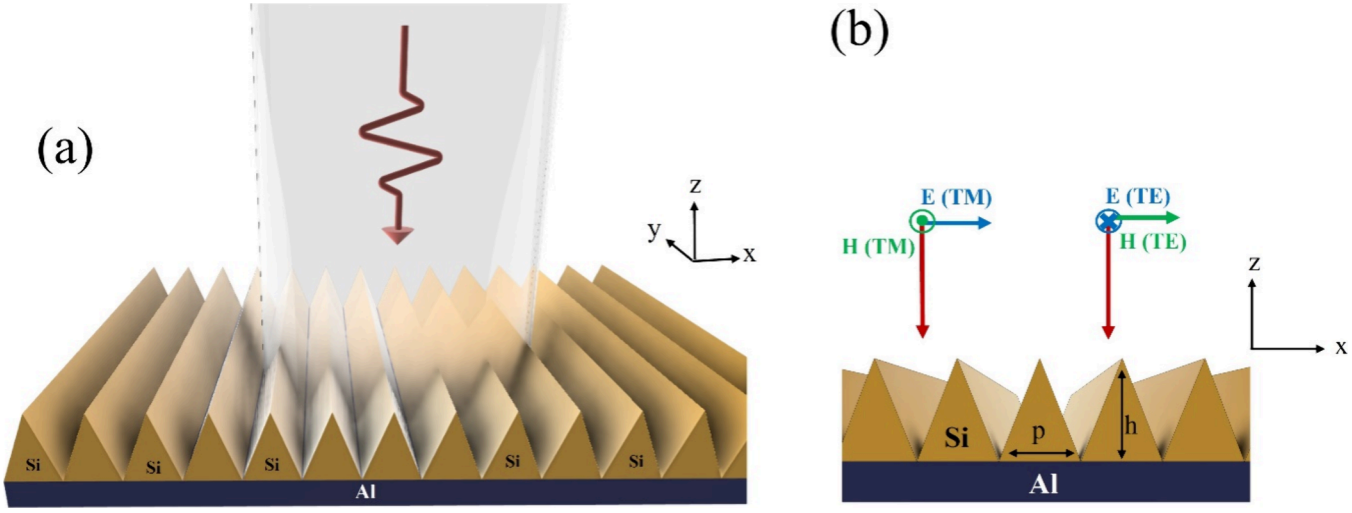


**Figure 1.** (a) 3D view and (b) cross-sectional view of the proposed design, consisting of a periodic array of triangular cross-sectioned Si nanorods over an Al back reflector. $p$ and $h$ denote the period and the height of nanorods, respectively. $p = 2$ $\mu$m and $h = 4$ $\mu$m. The directions of the electric (in blue) and magnetic (in green) fields for the TM and TE polarizations of the incident beam are also shown.

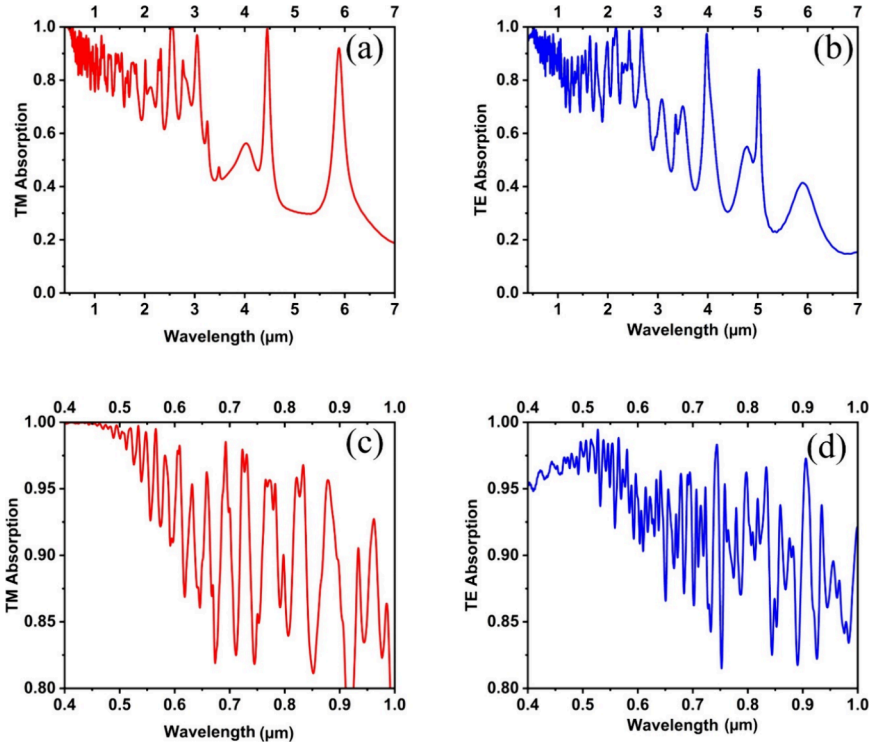


**Figure 2.** Absorption spectra for (a, c) TM and (b, d) TE polarizations at two different spectral ranges.

and electric dipole type Mie resonances are the physical reasons behind the TM and TE peaks, respectively. Such sensitivity performance underscores the effectiveness of our design[39] and exemplifies the broader principle demonstrated in this work, that is, utilizing multidimensional data can significantly enhance biosensing precision. To quantitatively establish this principle, we select four resonant peaks from the absorption profiles of transverse magnetic (TM) and transverse electric (TE) polarizations and employ ML techniques, namely the Ridge Regression modeling, to analyze their predictive power.[40−44] By systematically evaluating all possible combinations of these predictors (peaks)—from using each individually to incorporating all four simultaneously—we show that adding predictors consistently improves precision. Specifically, when combining the peaks from both polarizations, approximately 3 orders of magnitude enhancement in bulk refractive index detection precision is achieved compared to some single peaks. This approach allows us to maintain the same hardware—biosensor structure and measurement setup—while enhancing performance through innovative data processing. The findings presented in this paper not only highlight the desirable sensitivity performance of our multiresonant structure but also provide proof of concept for a general novel paradigm in biosensing. By demonstrating the synergy between multiresonance data acquisition and ML-


https://doi.org/10.1021/acsomega.5c01700
ACS Omega 2025, 10, 20713−20722

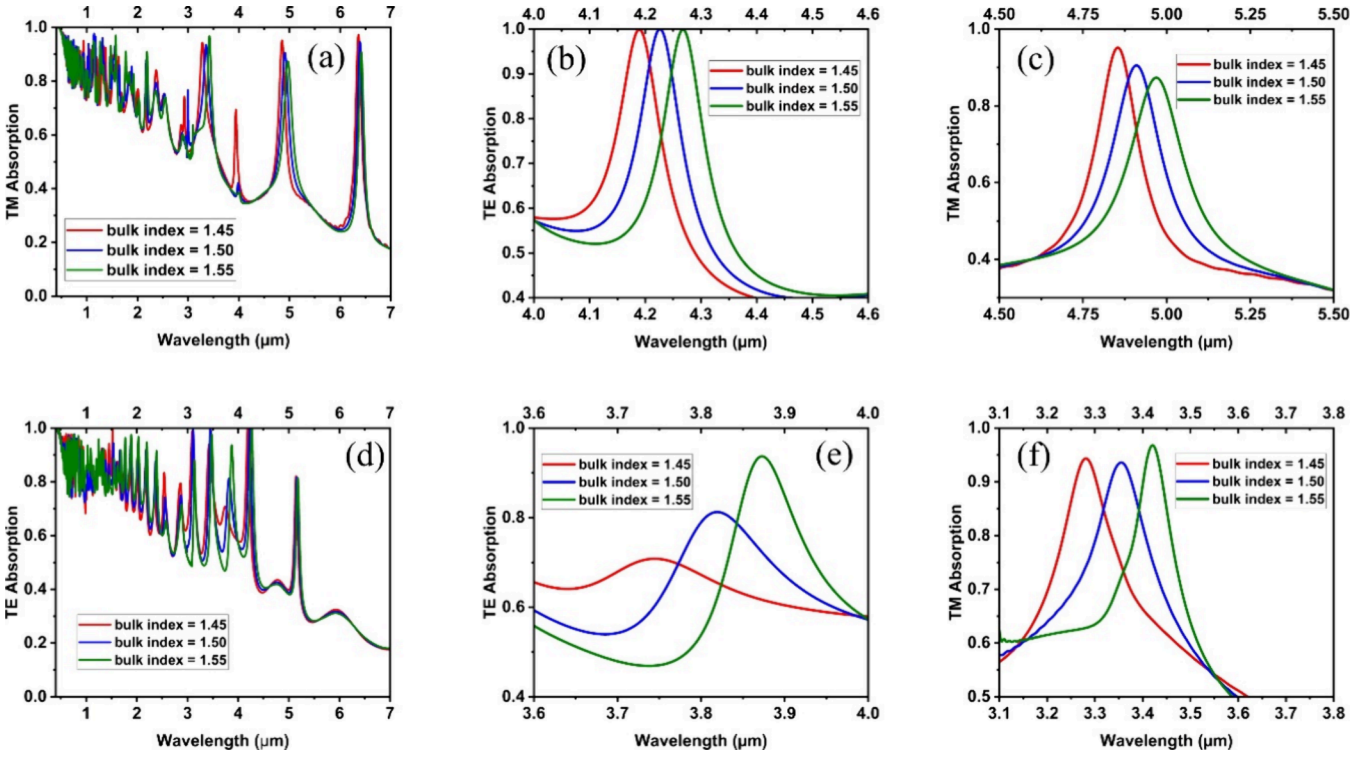


**Figure 3.** Absorption spectra for three different bulk refractive index values of 1.45, 1.50, and 1.55 for the (a−c) TM and (d−f) TE polarizations.

based analysis, this work lays the foundation for future advancements in high-precision biosensing technologies.

## 2. PROPOSED STRUCTURE

The schematic of the proposed structure is shown in Figure 1 along with the definition of the *xyz* coordinates. The structure consists of a periodic array of silicon based nanorods with triangular cross-section. Figure 1b demonstrates the cross-section (side view) of the structure, where it can be observed that the nanorods have a triangular shape in the cross section with the base (or array period), $p = 2$ $\mu$m, and height, $h = 4$ $\mu$m. The reason to use a tapered design instead of one with vertical sidewalls is that a tapered design is equivalent to superposition of various widths, each supporting a specific resonance, leading to maximization of the multiresonant behavior. The substrate is an optically thick Aluminum layer to ensure that all the transmission is blocked.

## 3. SIMULATION RESULTS

The reflection spectrum of the proposed structure is simulated. The simulations are carried out in the Finite-difference time-domain (FDTD) environment using the commercial Ansys Lumerical FDTD software, and the details of the simulation are mentioned in the Methods section. Since the transmission ($T$) is almost zero, the absorption spectrum ($A$) can be directly found from the reflection spectrum (R), *i.e.*, $A = 1 - R$, which is exemplified in Figure 2a and Figure 2b for the spectral range of 0.4−7 $\mu$m for the TM and TE polarizations, respectively. It can be seen that for both polarizations there are a high number of distinct peaks in the absorption spectrum, covering the infrared range. There are also a high number of peaks available in the wavelength range below 1 $\mu$m that cannot be seen very distinctly in Figure 2a,b. Therefore, Figure 2c,d show the TM and TE absorption spectra of the structure in the 0.4−1 $\mu$m spectral range to demonstrate the peaks in that range more clearly. However, for simplicity, in the rest of this work, the peaks in the infrared range are used to demonstrate the concept.

To evaluate the biosensing functionality of the structure, we examine the peak shift with varying bulk refractive index above the structure. Figure 3a shows the absorption spectra of the TM polarization for the three bulk refractive index values of 1.45, 1.50, and 1.55. It can be observed that the peaks undergo a red shift (toward higher wavelengths) as the bulk refractive index increases. For example, Figure 3b shows the close-up view of the shift of the absorption peak around the wavelength of 3.3 $\mu$m. It can be observed that the peak shifts around 139.2 nm for a 0.1 increment in the bulk index (from 1.45 to 1.55), corresponding to a bulk sensitivity of 1392 nm/RIU for this peak. Another example of a TM polarization peak with high sensitivity is the one around the wavelength of 4.8 $\mu$m which has a bulk sensitivity of 1149 nm/RIU, shown in Figure 3c (See Table 1 for more peak sensitivity examples for both polarizations).

Figure 3d shows the absorption spectra shift of the TE polarization for the bulk refractive index values of 1.45, 1.50,

**Table 1. nm/RIU for the Peak Shifts in Figure 4[a]**

| TM polarization | | TE polarization | |
|---|---|---|---|
| peak location (nm)[1] | sensitivity (nm/RIU) | peak location (nm) | sensitivity (nm/RIU) |
| 1859 | 598 | 2349 | 394 |
| 2926 | 1706 | 3428 | 502 |
| 3281 | 1392 | 3744 | 1283 |
| 4854 | 1149 | 4189 | 784 |

[a]The peak locations (in nm) mentioned in the table refer to their locations at the bulk index of 1.45.



https://doi.org/10.1021/acsomega.5c01700
ACS Omega 2025, 10, 20713−20722

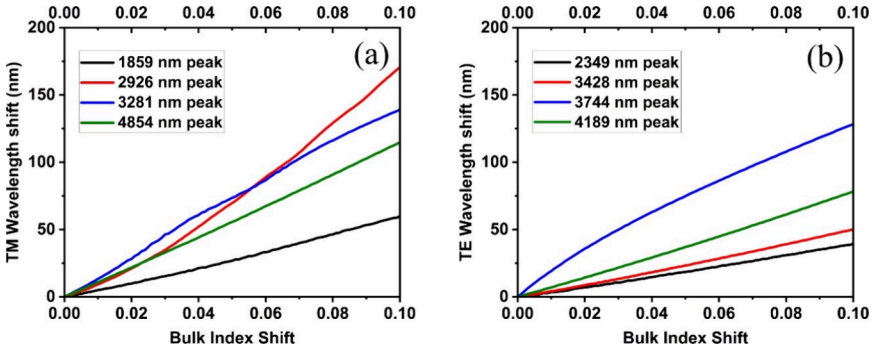


**Figure 4.** Resonance wavelength shift vs bulk index change for the structure for four peaks of (a) TM and (b) TE polarization. The peak locations (in nm) mentioned in the figure refer to their location at a bulk index of 1.45.

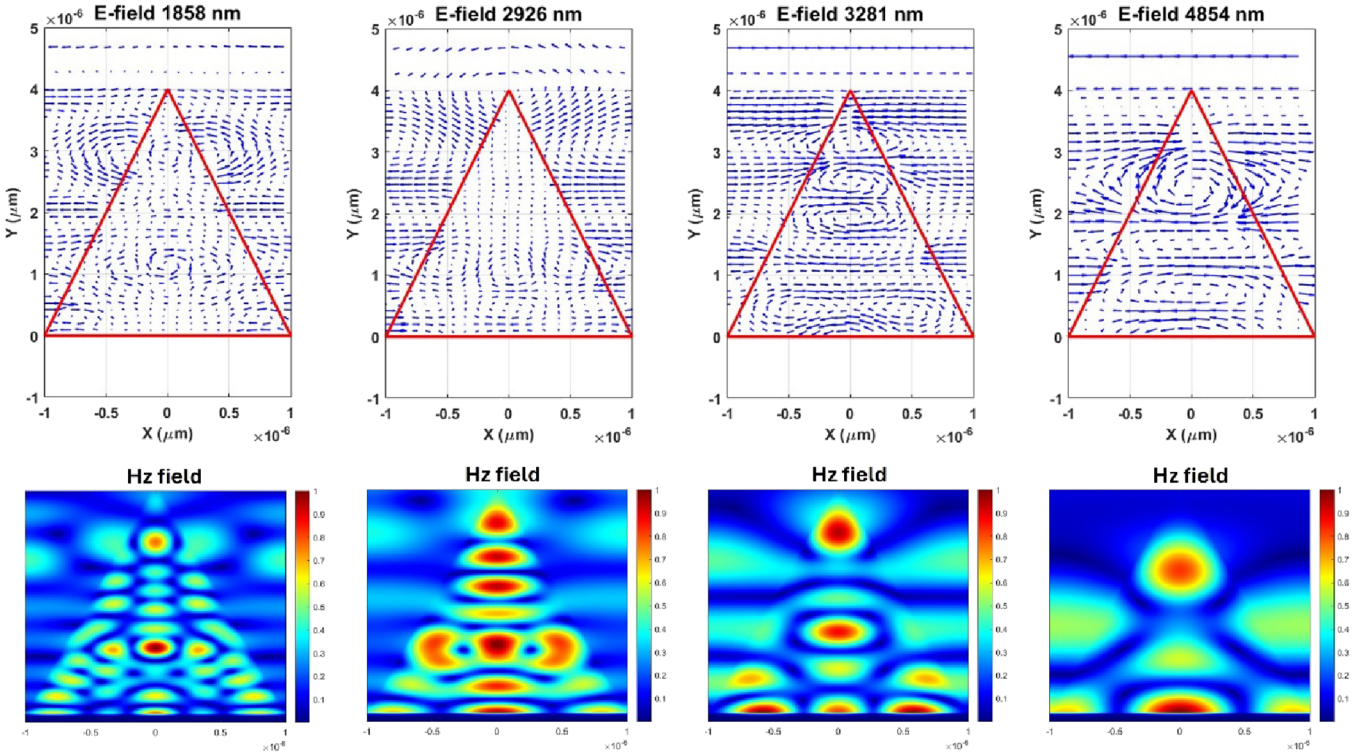


**Figure 5.** E-field quiver maps (top panel) and $H_z$ field magnitude color maps (bottom panel) of the TM 4 peaks selected for analysis listed in Table 1.

and 1.55. Figure 3e shows the close-up view of the shift of the absorption peak around the wavelength of 3.5 $\mu$m, which has a bulk sensitivity of 1283 nm/RIU. Another example is the peak around the wavelength of 4.2 $\mu$m. The bulk sensitivity is calculated to be around 784 nm/RIU for this peak. Unlike other designs requiring intricate multilayered nanofabrication, our design achieves a high sensitivity performance with enhanced simplicity and scalability.

By comparing the peak shifts for both polarizations, we can see that almost all the peaks for the TM polarization undergo a stronger red-shift compared to the TE polarization. This is due to the fact that the electric field is parallel to the cross-section plane for the TM polarization, and hence it penetrates directly into the surface of the Si triangular nanorods (see Figure 1b). Therefore, the electric resonances for the TM polarization can be influenced more significantly by the index variation above the surface of the structure. This is while for the TE polarization, the electric field is perpendicular to the cross-section, *i.e.*, parallel to the surface of triangular nanorods, making the electric resonances less sensitive to index variations.

To evaluate the refractive index sensitivity of the structure more closely, we vary the refractive index of the simulation environment, from 1.45 to 1.55 by 0.001 increments. For the TM and TE polarizations, certain peaks shown in Figure 3a and Figure 3d are chosen, respectively, and the wavelength shift versus the bulk index shift are plotted for those peaks. The results are shown in Figure 4a,b for the TM and TE polarizations, respectively. The nm/RIU for the peak shifts in Figure 4 are presented in Table 1.

As seen in Figure 4, like most biosensing measurements, the relationship between the measured quantity (peak shift) and the sensing input (bulk index) seems linear. However, even in the simulations, the relationships are not perfectly linear due to nonlinear physical phenomena such as adjacent resonances or peaks influencing each other. In actual experimental measure-


https://doi.org/10.1021/acsomega.5c01700
ACS Omega 2025, 10, 20713−20722

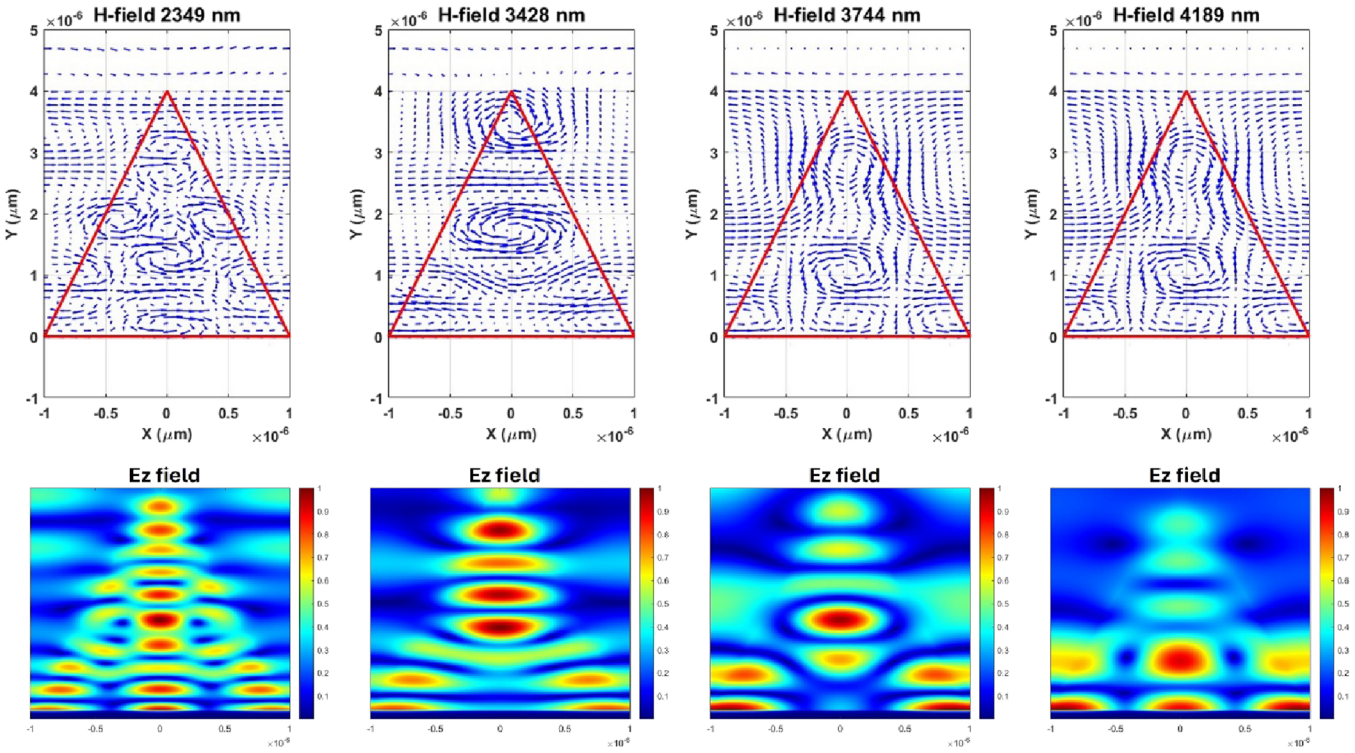


**Figure 6.** H-field quiver maps (top panel) and $E_z$ field magnitude color maps (bottom panel) of the TE 4 peaks selected for analysis listed in Table 1.

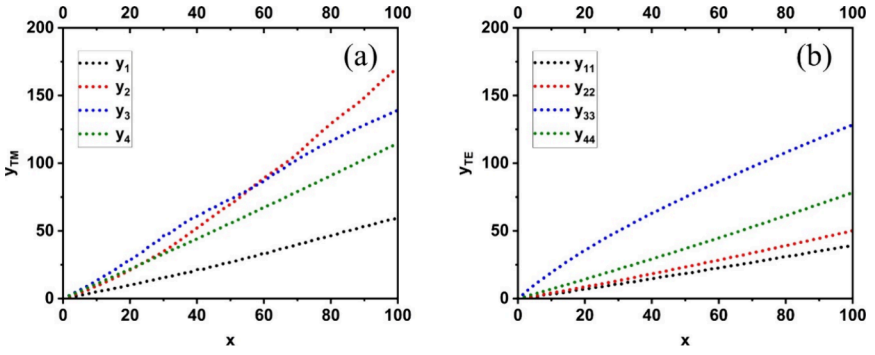


**Figure 7.** Scatter plots of $y_i$'s vs $x$, referring to the peaks chosen from the (a) TM and (b) TE absorption spectra vs bulk index change (1000×).

ments, the linearity may be even weaker due to experimental imperfections and errors such as noise or measurement setup inaccuracies. Therefore, a purely linear model does not always provide a precise prediction of the bulk index value based on the measured resonance location. This occurs when only one peak shift is considered, and a linear fit is used as the calibration curve. However, as will be demonstrated in detail in the coming sections, if, through data training and machine learning algorithms, more than one peak (in this case 4 peaks) is considered, the precision of estimating the bulk index based on the measured peak location gets significantly enhanced. In other words, if we use multiple peaks or resonances, or a multidimensional set of data (4D in this case), instead of one peak, or using 1D data, the precision of the system will be highly improved. This enables us to attain significantly higher precision using the same biosensor structure and the same measurement setup, but with a slightly different post data processing strategy.

Figures 5 and 6 present the electric and magnetic field distributions for the selected TM and TE polarization resonances, respectively, providing strong confirmation of Mie-type dipole modes within the silicon nanorod.[45] For TM polarization (Figure 5), where the incident wave consists of $E_x$ and $H_z$, the fields inside the structure include $E_x$, $E_y$, and $H_z$. The bottom row of Figure 5 illustrates the localized $H_z$ hotspots, while the top row presents quiver plots of $E_x$–$E_y$, revealing clear circulating electric field loops around the magnetic field peaks. This behavior aligns with Ampère's Law, $\nabla \times E = -\partial B/\partial t$, where a time-varying $H_z$ dipole moment along the $z$-axis induces a rotational $E_x$, $E_y$ field around it. The presence of these closed-loop electric field structures around a concentrated magnetic field hotspot confirms that these resonances correspond to magnetic dipole Mie modes.

Similarly, Figure 6 (TE polarization) shows the field behavior for an incident wave consisting of $H_x$ and $E_z$, with the fields inside the nanorod including $H_x$, $H_y$, and $E_z$. The bottom row illustrates the localized $E_z$ field hotspots, while the


https://doi.org/10.1021/acsomega.5c01700
ACS Omega 2025, 10, 20713−20722

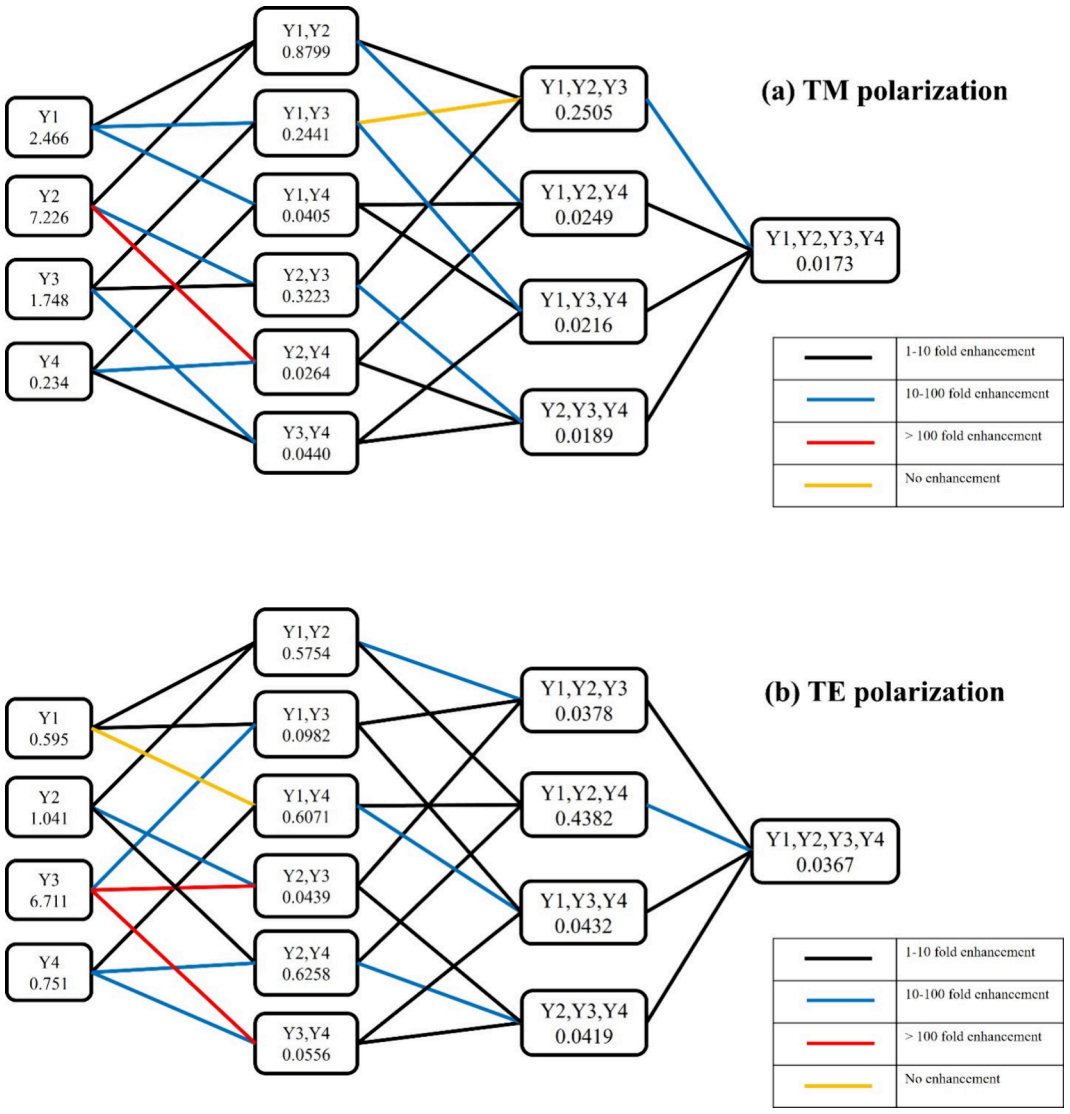


**Figure 8.** MSE diagram comparing the accuracy performance of Ridge Regression modeling using all possible combinations of the four predictors for (a) TM and (b) TE polarizations.

top row quiver maps display circulating $H_x$, $H_y$ vectors around these regions. This pattern is characteristic of Faraday's Law, $\nabla \times H = \partial D/\partial t$, where an oscillating electric dipole moment along the $z$-axis ($E_z$) induces a surrounding rotational magnetic field ($H_x$, $H_y$). The formation of these looped H-field structures around strong $E_z$ hotspots confirms that these TE resonances correspond to electric dipole Mie modes.

Together, these field distributions validate that TM polarization supports magnetic dipole Mie resonances, while TE polarization supports electric dipole Mie resonances, fully consistent with the expected behavior of high-index dielectric nanostructures in the infrared. The presence of well-defined dipole fields and circulating response patterns further reinforce that these resonances originate from localized Mie-type scattering rather than extended traveling waves or guided waves, governing the observed refractive index sensitivity trends. This is supported by the strong field confinement near the nanorod and the absence of extended mode profiles typical of leaky waveguide modes.

## 4. MULTIRESONANCE DATA PROCESSING THROUGH ML AND PRECISION ENHANCEMENT

To demonstrate the biosensing precision enhancement through ML based multidimensional data processing, we consider the shift of 4 TM and 4 TE peaks shown in Figure 4a and Figure 4b, respectively. Figure 7a and Figure7b demonstrate the scatter plots of the shift of those 4 peaks for TM and TE polarizations, respectively, versus the bulk index shift starting from 1.45. The bulk index shift ranging between 0.001 to 0.1 with 0.001 increments is multiplied by 1000 for simplicity, and is denoted as $x$, *i.e.*, 100 values in total, ranging from 1 to 100. The peak shift values are referred to as $y_1$, $y_2$, $y_3$, and $y_4$ for the TM peaks at the wavelengths of 1859, 2926, 3281, and 4854 nm, respectively, and as $y_{11}$, $y_{22}$, $y_{33}$, and $y_{44}$ for the TE peaks at the wavelengths of 2349, 3428, 3744, and 4189 nm, respectively. Since $y$ values (peak shifts) are measured in the biosensor (the location of peaks) and are used to predict the value of $x$ associated with them (bulk index shift), $y_i$'s are referred to as predictors, and $x$ is referred to as the target variable. Table S1 in the Supporting Information shows the descriptive statistics of the target variable $x$ and the


https://doi.org/10.1021/acsomega.5c01700
ACS Omega 2025, 10, 20713−20722

TM polarization predictors. The model development for ML based data training is detailed in the Supporting Information, using the TM polarization predictors for demonstration. During model development, we conducted multicollinearity assessments and calculated Variance Inflation Factors (VIF) to ensure predictor robustness. VIF values suggested strong multicollinearity among predictors. Therefore, in addition to the linear regression used for multidimensional modeling initially, we have used a Ridge Regression model to address possible adverse effects of multicollinearity in multidimensional data modeling. Additionally, all models underwent rigorous validation using 10-fold cross-validation to ensure reliability and generalizability.

Figure 8 illustrates the performance enhancement achieved by leveraging multiple resonance shifts in the proposed multiresonance optical biosensor for bulk refractive index sensing. The diagrams in Figure 8a,b are organized to depict all possible combinations of predictors $y_1$, $y_2$, $y_3$, and $y_4$, and their associated mean squared error (MSE) values using the Ridge Regression modeling for the TM and TE polarizations, respectively. The leftmost column represents the individual predictors ("$y_1$" through "$y_4$") and their corresponding MSE when used individually in simple 1D linear modeling. As we move rightward, the combinations of the predictors increase, culminating in the simultaneous utilization of all four predictors. Each box is labeled with its respective MSE value, showcasing the performance of that specific combination of predictors.

The progression from left to right consistently demonstrates a reduction in MSE values as additional predictors are incorporated. For instance, in the TM polarization, two peaks used individually yield MSE values of 2.466 and 7.226, respectively. However, when all four TM peaks are utilized together, the MSE dramatically reduces to 0.0173. Similarly, in the TE polarization, individual MSEs of 1.1186 and 7.3318 are reduced to 0.0357 when all four TE peaks are combined. Importantly, by incorporating both TM and TE polarizations and utilizing all eight resonant peaks as 8-dimensional data, the MSE further improves to 0.0090, with an $R^2$ value of 1.000, demonstrating near-perfect precision.

The lines between the columns connect the combinations in the right columns that can be produced by their connected adjacent left columns by adding another predictor to it. There are 28 connecting lines in total. The red line highlights combinations where the inclusion of additional predictors results in a two-order-of-magnitude improvement in MSE. For instance, for TM polarization, combining "$y_2$" and "$y_3$" leads to a 274-fold precision gain compared to using "$y_2$" alone. There are in total 9 blue lines which indicate at least 1 order of magnitude improvement, while black lines represent MSE enhancements ranging between 1 and 10 times. This means for a total of 10 out of 28 lines, adding an additional predictor to certain predictor combinations, leads to at least an order of magnitude enhancement in the modeling precision for the case of TM polarization, which is over 35% of all the lines. For the case of TE polarization, there are 2 red lines (>100-fold enhancement) and 8 blue lines (>10-fold enhancement), indicating a similar precision enhancement performance compared to the TM polarization. The yellow lines represent combinations where the inclusion of additional predictors results in no improvement. There is only one yellow line for each of the TM and TE polarizations in Figure 8a,b, out of a total of 28 cases, where in both cases MSE has remained approximately the same. It can therefore be observed that additional predictors have nonlinear impact. While the overall trend is a reduction in MSE with more predictors, the magnitude of improvement varies. For example, the addition of "$y_4$" to "$y_1$" and "$y_3$" (indicated by black lines) provides less significant improvement compared to the addition of "$y_2$" to "$y_1$" (red line) for the TM polarization.

The findings illustrated by the figure confirm that multiresonance analysis significantly enhances biosensing precision without requiring additional hardware. This improvement stems solely from advanced postprocessing using machine learning. The systematic reduction in MSE demonstrates the ability of machine learning techniques to extract synergistic information from multiple resonance shifts, effectively overcoming limitations of traditional single-resonance methods.

Figure 8, as a complete picture, further emphasizes the cost-effectiveness of the proposed methodology. Traditional methods rely on hardware advancements to improve sensing precision, often leading to increased costs and complexity. In contrast, this approach achieves superior performance solely through data-driven techniques applied to existing hardware. This paradigm shift not only reduces costs but also broadens the applicability of high-precision biosensors in resource-constrained settings.

Finally, combining all the peaks in both TE and TM polarizations, *i.e.*, using 8 dimensional data in our Ridge Regression model, the MSE and $R^2$ values of 0.009 and 1.000 are achieved, respectively. This further attests to the enhancement of accuracy in data modeling when all the predictors are incorporated. Other parameters associated with the 8-dimensional modeling are available in the Supporting Information.

## 5. DISCUSSION, CONCLUSIONS, AND FUTURE WORK

This study establishes a significant advancement in the field of biosensing by demonstrating the transformational potential of utilizing multidimensional data in multiresonance biosensors. The results provide compelling evidence that the integration of multiple predictors significantly enhances the precision of target variable prediction. By using a simple yet highly effective optical multiresonant structure as an illustrative example, we show that the principle of multidimensional data utilization is not only theoretically sound but also practically achievable with scalable fabrication techniques. In practical implementations, this grating structure can be fabricated using nanoimprint lithography with prepatterned molds designed to yield triangular profiles.[46] Other viable methods include electron beam lithography followed by anisotropic etching,[46] or angled ion beam etching to create tapered sidewalls.[47] While a comprehensive comparison of fabrication strategies is beyond the scope of this study, the simplicity of the unit cell design ensures strong compatibility with scalable manufacturing technologies.

Our structure, consisting of a triangular cross-section array of periodic silicon nanorods over an aluminum back reflector, exemplifies a design that combines simplicity with high performance. The sensitivity of the structure, which can be as high as 1706 nm/RIU, underscores its capability as a biosensing platform. This performance is further elevated when the multidimensional nature of its resonances is leveraged through machine learning methods. By systematically analyzing combinations of four resonant predictors using Ridge Regression modeling, we reveal a clear trend: the inclusion of additional predictors leads to consistent improvements in


https://doi.org/10.1021/acsomega.5c01700
ACS Omega 2025, 10, 20713−20722

precision, with some combinations achieving over an order of magnitude reduction in mean squared error.

Notably, for TM polarization, individual peaks result in MSEs of 2.466 and 7.226, while the use of all four peaks reduces the MSE to 0.0173. Similarly, for TE polarization, the individual MSEs of 1.1186 and 7.3318 are reduced to 0.0357 when all four peaks are combined. Furthermore, combining TM and TE polarizations and utilizing all eight resonant peaks results in the best performance observed in this study, with an MSE of 0.0090 and an $R^2$ value of 1.000. This highlights the high potential of maintaining the same biosensor structure and measurement setup while enhancing performance through advanced data processing techniques. This approach represents a novel and efficient pathway to significantly improve biosensing precision without the need for complex hardware modifications.

The ability to achieve near-perfect precision with a simple biosensor design and advanced data processing renders this work particularly promising for complex and real-time biosensing applications. The significant enhancement in data interpretation accuracy demonstrated here is critical for addressing the challenges of high-speed and high-complexity biosensing environments. By providing a robust framework for leveraging multidimensional data, this work paves the way for biosensing platforms capable of tackling intricate biological systems and dynamic scenarios. Compared to colorimetric assays,[48] which rely on chromogenic reactions and often suffer from limited sensitivity and subjectivity in interpretation, the spectra-based bulk index sensing approach enables quantitative, label-free detection with higher precision. Furthermore, unlike electrochemical methods[49] that may require redox-active species and suffer from electrode fouling, our proposed index sensing based system remains robust and scalable, with sensing performance enhanced solely through postprocessing and ML.

The implications of these findings extend beyond the specific design and application studied here. They represent a general principle that can be applied to a wide range of biosensing technologies. Multidimensional data acquisition, when coupled with advanced data analysis techniques such as machine learning, offers a powerful pathway to overcoming the limitations of traditional one-dimensional biosensing approaches. This paradigm shift has the potential to significantly enhance the accuracy, reliability, and robustness of biosensors across diverse applications.

Looking ahead, the integration of multiresonance biosensors with sophisticated ML algorithms opens new avenues for innovation in biosensing. Future research could explore the application of this principle to more complex biological systems, incorporate additional predictors from other physical modalities, and develop advanced machine learning frameworks tailored for biosensing data. By advancing the understanding and application of multidimensional data utilization, this work contributes to the ongoing evolution of biosensing technologies and their impact on science and society.

## 6. METHODS

**Lumerical Simulation Setup.** The simulation is carried out in the FDTD simulation environment using the Ansys Lumerical commercial software. The simulation environment is 2D in the *xy* plane since the structure is infinite in the *z* axis direction. In other words, only the cross section of one period of the structure is being simulated. The boundary condition in the *x* axis direction is the periodic boundary condition, while along the *y* axis it is chosen to be the perfectly matched layer (PML) boundary condition to ensure no reflection back in that direction. The Frequency-Domain Field Profile DFT monitor is placed right under the top boundary of the FDTD simulation environment, and the planewave source is placed under the monitor. The monitor collects the reflection data. The monitor has 30,000 frequency points and collects the spectrum in the 0.4−10 $\mu$m range. The planewave source is incident in the $-y$ direction for the normal incidence.

For the field simulations, the monitor was placed in the *xy* plane in the simulation environment. The field simulations are carried out with the 1.45 bulk index since the resonant behavior of certain peaks may disappear while changing the bulk index from 1 to 1.45.

## ■ ASSOCIATED CONTENT

### Supporting Information

The Supporting Information is available free of charge at https://pubs.acs.org/doi/10.1021/acsomega.5c01700.

Descriptive statistics of all variables for the TM polarization (Table S1), correlation analysis (Table S2), 10-fold cross validation, simple 1D linear regression models (Table S3), multi-dimensional modeling approaches (Tables S4 and S5 and Figures S1−S4), 4D Ridge Regression coefficients for the TM polarization (Table S6), 8-dimensional Ridge Regression modeling parameters (Figures S7 and S8), and feature selection (PDF)

## ■ AUTHOR INFORMATION


### Corresponding Author

**Xudong Fan** − *Department of Biomedical Engineering, Center for Wireless Integrated MicroSensing and Systems (WIMS2), and Max Harry Weil Institute for Critical Care Research and Innovation, University of Michigan, Ann Arbor, Michigan 48109, United States;* orcid.org/0000-0003-0149-1326; Email: xsfan@umich.edu

### Authors

**Majid Aalizadeh** − *Department of Biomedical Engineering, Department of Electrical Engineering and Computer Science, Center for Wireless Integrated MicroSensing and Systems (WIMS2), and Max Harry Weil Institute for Critical Care Research and Innovation, University of Michigan, Ann Arbor, Michigan 48109, United States;* orcid.org/0000-0002-4312-1940

**Morteza Azmoudeh Afshar** − *Informatics Institute, Istanbul Technical University, Istanbul 34485, Turkey*

Complete contact information is available at: https://pubs.acs.org/10.1021/acsomega.5c01700


### Notes

The authors declare no competing financial interest.

## ■ ACKNOWLEDGMENTS

The authors thank the support from National Science Foundation under 2225568. One of the authors (M.A.) thanks Abdur-Raheem Al-Hallak for the discussions about peak detection.

## REFERENCES


(1) Chen, C.; Wang, J. Optical biosensors: an exhaustive and comprehensive review. *Analyst* **2020**, *145* (5), 1605−1628.
(2) Chen, Y. T.; Lee, Y. C.; Lai, Y. H.; Lim, J. C.; Huang, N. T.; Lin, C. T.; Huang, J. J. Review of Integrated Optical Biosensors for Point-Of-Care Applications. *Biosensors* **2020**, *10* (12), 209.
(3) Kaur, B.; Kumar, S.; Kaushik, B. K. Recent advancements in optical biosensors for cancer detection. *Biosens Bioelectron* **2022**, *197*, No. 113805.
(4) Richter, F. U.; Sinev, I.; Zhou, S.; Leitis, A.; Oh, S. H.; Tseng, M. L.; Kivshar, Y.; Altug, H. Gradient High-Q Dielectric Metasurfaces for Broadband Sensing and Control of Vibrational Light-Matter Coupling. *Adv. Mater.* **2024**, *36* (25), No. e2314279.
(5) Zhang, Z.; Yang, M.; Yan, X.; Guo, X.; Li, J.; Yang, Y.; Wei, D.; Liu, L.; Xie, J.; Liu, Y.; et al. The Antibody-Free Recognition of Cancer Cells Using Plasmonic Biosensor Platforms with the Anisotropic Resonant Metasurfaces. *ACS Appl. Mater. Interfaces* **2020**, *12* (10), 11388−11396.
(6) Zhang, C.; Xue, T.; Zhang, J.; Liu, L.; Xie, J.; Wang, G.; Yao, J.; Zhu, W.; Ye, X. Terahertz toroidal metasurface biosensor for sensitive distinction of lung cancer cells. *Nanophotonics* **2021**, *11* (1), 101−109.
(7) Tittl, A.; John-Herpin, A.; Leitis, A.; Arvelo, E. R.; Altug, H. Metasurface-Based Molecular Biosensing Aided by Artificial Intelligence. *Angew. Chem., Int. Ed. Engl.* **2019**, *58* (42), 14810−14822.
(8) Homola, J. Present and future of surface plasmon resonance biosensors. *Anal Bioanal Chem.* **2003**, *377* (3), 528−539.
(9) Wang, Q.; Ren, Z. H.; Zhao, W. M.; Wang, L.; Yan, X.; Zhu, A. S.; Qiu, F. M.; Zhang, K. K. Research advances on surface plasmon resonance biosensors. *Nanoscale* **2022**, *14* (3), 564−591.
(10) Jaksic, Z.; Vukovic, S.; Matovic, J.; Tanaskovic, D. Negative Refractive Index Metasurfaces for Enhanced Biosensing. *Materials (Basel)* **2011**, *4* (1), 1−36.
(11) Konopsky, V. N.; Alieva, E. V. A biosensor based on photonic crystal surface waves with an independent registration of the liquid refractive index. *Biosens Bioelectron* **2010**, *25* (5), 1212−1216.
(12) Perera, C.; Vernon, K.; Cheng, E.; Sathian, J.; Jaatinen, E.; Davis, T. Highly compact refractive index sensor based on stripe waveguides for lab-on-a-chip sensing applications. *Beilstein J. Nanotechnol* **2016**, *7*, 751−757.
(13) White, I. M.; Fan, X. On the performance quantification of resonant refractive index sensors. *Opt Express* **2008**, *16* (2), 1020−1028.
(14) Shangguan, Q.; Chen, Z.; Yang, H.; Cheng, S.; Yang, W.; Yi, Z.; Wu, X.; Wang, S.; Yi, Y.; Wu, P. Design of Ultra-Narrow Band Graphene Refractive Index Sensor. *Sensors* **2022**, *22* (17), 6483.
(15) Haque, E.; Anwar Hossain, M.; Namihira, Y.; Ahmed, F. Microchannel-based plasmonic refractive index sensor for low refractive index detection. *Appl. Opt.* **2019**, *58* (6), 1547−1554.
(16) Fan, X.; White, I. M.; Shopova, S. I.; Zhu, H.; Suter, J. D.; Sun, Y. Sensitive optical biosensors for unlabeled targets: a review. *Anal. Chim. Acta* **2008**, *620* (1−2), 8−26.
(17) Shen, Z.; Du, M. High-performance refractive index sensing system based on multiple Fano resonances in polarization-insensitive metasurface with nanorings. *Opt Express* **2021**, *29* (18), 28287−28296.
(18) Yan, Z.; Yan, S.; Xu, Z.; Chen, C.; Cao, Y.; Yan, X.; Wang, C.; Wu, T. Multi-Structure-Based Refractive Index Sensor and Its Application in Temperature Sensing. *Sensors* **2025**, *25* (2), 412.
(19) Guchhait, S.; Chatterjee, S.; Chakravarty, T.; Ghosh, N. A metal-insulator-metal waveguide-based plasmonic refractive index sensor for the detection of nanoplastics in water. *Sci. Rep* **2024**, *14* (1), 21495.
(20) Shen, Y.; Zhou, J.; Liu, T.; Tao, Y.; Jiang, R.; Liu, M.; Xiao, G.; Zhu, J.; Zhou, Z. K.; Wang, X.; et al. Plasmonic gold mushroom arrays with refractive index sensing figures of merit approaching the theoretical limit. *Nat. Commun.* **2013**, *4*, 2381.
(21) Jágerská, J.; Zhang, H.; Diao, Z.; Thomas, N. L.; Houdré, R. Refractive index sensing with an air-slot photonic crystal nanocavity. *Opt. Lett.* **2010**, *35* (15), 2523−2525.
(22) Lodewijks, K.; Van Roy, W.; Borghs, G.; Lagae, L.; Van Dorpe, P. Boosting the figure-of-merit of LSPR-based refractive index sensing by phase-sensitive measurements. *Nano Lett.* **2012**, *12* (3), 1655−1659.
(23) Liu, Y.; Zhou, W.; Sun, Y. Optical Refractive Index Sensing Based on High-Q Bound States in the Continuum in Free-Space Coupled Photonic Crystal Slabs. *Sensors* **2017**, *17* (8), 1861.
(24) Maksimov, D. N.; Gerasimov, V. S.; Romano, S.; Polyutov, S. P. Refractive index sensing with optical bound states in the continuum. *Opt Express* **2020**, *28* (26), 38907−38916.
(25) Akkilic, N.; Geschwindner, S.; Hook, F. Single-molecule biosensors: Recent advances and applications. *Biosens Bioelectron* **2020**, *151*, No. 111944.
(26) Sin, M. L.; Mach, K. E.; Wong, P. K.; Liao, J. C. Advances and challenges in biosensor-based diagnosis of infectious diseases. *Expert Rev. Mol. Diagn* **2014**, *14* (2), 225−244.
(27) Rodrigo, D.; Tittl, A.; Ait-Bouziad, N.; John-Herpin, A.; Limaj, O.; Kelly, C.; Yoo, D.; Wittenberg, N. J.; Oh, S. H.; Lashuel, H. A.; et al. Resolving molecule-specific information in dynamic lipid membrane processes with multi-resonant infrared metasurfaces. *Nat. Commun.* **2018**, *9* (1), 2160.
(28) Geng, Z.; Wang, Z.; Liu, C. Route to flexible metamaterial terahertz biosensor based on multi-resonance dips. *Opt Express* **2022**, *30* (15), 27418−27428.
(29) Choi, C. J.; Semancik, S. Multi-resonant plasmonic nanodome arrays for label-free biosensing applications. *Nanoscale* **2013**, *5* (17), 8138−8145.
(30) Chen, C.; Wagn, K.; Hou, X. Characterizing amyloid protein conformation with a multi-resonant metasurface based biosensor in the infrared window. *Opt Express* **2024**, *32* (4), 5287−5300.
(31) Chang, Y. T.; Lai, Y. C.; Li, C. T.; Chen, C. K.; Yen, T. J. A multi-functional plasmonic biosensor. *Opt Express* **2010**, *18* (9), 9561−9569.
(32) Banerjee, A.; Maity, S.; Mastrangelo, C. H. Nanostructures for Biosensing, with a Brief Overview on Cancer Detection, IoT, and the Role of Machine Learning in Smart Biosensors. *Sensors* **2021**, *21* (4), 1253.
(33) Cui, F.; Yue, Y.; Zhang, Y.; Zhang, Z.; Zhou, H. S. Advancing Biosensors with Machine Learning. *ACS Sens* **2020**, *5* (11), 3346−3364.
(34) Kokabi, M.; Tahir, M. N.; Singh, D.; Javanmard, M. Advancing Healthcare: Synergizing Biosensors and Machine Learning for Early Cancer Diagnosis. *Biosensors* **2023**, *13* (9), 884.
(35) Schackart, K. E., 3rd; Yoon, J. Y. Machine Learning Enhances the Performance of Bioreceptor-Free Biosensors. *Sensors* **2021**, *21* (16), 5519.
(36) Zhang, K.; Wang, J.; Liu, T.; Luo, Y.; Loh, X. J.; Chen, X. Machine Learning-Reinforced Noninvasive Biosensors for Healthcare. *Adv. Healthc Mater.* **2021**, *10* (17), No. e2100734.
(37) Lavin, A.; Vicente, J.; Holgado, M.; Laguna, M. F.; Casquel, R.; Santamaria, B.; Maigler, M. V.; Hernandez, A. L.; Ramirez, Y. On the Determination of Uncertainty and Limit of Detection in Label-Free Biosensors. *Sensors* **2018**, *18* (7), 2038.
(38) Duan, X.; Li, Y.; Rajan, N. K.; Routenberg, D. A.; Modis, Y.; Reed, M. A. Quantification of the affinities and kinetics of protein interactions using silicon nanowire biosensors. *Nat. Nanotechnol* **2012**, *7* (6), 401−407.
(39) Chen, H.; Chen, Z.; Yang, H.; Wen, L.; Yi, Z.; Zhou, Z.; Dai, B.; Zhang, J.; Wu, X.; Wu, P. Multi-mode surface plasmon resonance absorber based on dart-type single-layer graphene. *RSC Adv.* **2022**, *12* (13), 7821−7829.
(40) Flynn, C. D.; Chang, D. Artificial Intelligence in Point-of-Care Biosensing: Challenges and Opportunities. *Diagnostics* **2024**, *14* (11), 1100.
(41) Ianni, J. D.; Cao, Z.; Grissom, W. A. Machine learning RF shimming: Prediction by iteratively projected ridge regression. *Magn Reson Med.* **2018**, *80* (5), 1871−1881.
(42) Hassan, M. M.; Xu, Y.; Sayada, J.; Zareef, M.; Shoaib, M.; Chen, X.; Li, H.; Chen, Q. Progress of machine learning-based



https://doi.org/10.1021/acsomega.5c01700
*ACS Omega* 2025, 10, 20713−20722

biosensors for the monitoring of food safety: A review. *Biosens Bioelectron* **2025**, *267*, No. 116782.
(43) de Vlaming, R.; Groenen, P. J. F. The Current and Future Use of Ridge Regression for Prediction in Quantitative Genetics. *BioMed Res. Int.* **2015**, *2015*, No. 143712.
(44) Arashi, M.; Roozbeh, M.; Hamzah, N. A.; Gasparini, M. Ridge regression and its applications in genetic studies. *PLoS One* **2021**, *16* (4), No. e0245376.
(45) Aalizadeh, M.; Serebryannikov, A. E.; Ozbay, E.; Vandenbosch, G. A. E. A simple Mie-resonator based meta-array with diverse deflection scenarios enabling multifunctional operation at near-infrared. *Nanophotonics* **2020**, *9* (15), 4589−4600.
(46) Zhu, C.; Ekinci, H.; Pan, A.; Cui, B.; Zhu, X. Electron beam lithography on nonplanar and irregular surfaces. *Microsyst Nanoeng* **2024**, *10*, 52.
(47) Desbiolles, B. X. E.; Bertsch, A.; Renaud, P. Ion beam etching redeposition for 3D multimaterial nanostructure manufacturing. *Microsyst Nanoeng* **2019**, *5*, 11.
(48) Pan, X.; Zhang, Z.; Yun, Y.; Zhang, X.; Sun, Y.; Zhang, Z.; Wang, H.; Yang, X.; Tan, Z.; Yang, Y.; et al. Machine Learning-Assisted High-Throughput Identification and Quantification of Protein Biomarkers with Printed Heterochains. *J. Am. Chem. Soc.* **2024**, *146* (28), 19239−19248.
(49) Zhu, C.; Yang, G.; Li, H.; Du, D.; Lin, Y. Electrochemical sensors and biosensors based on nanomaterials and nanostructures. *Anal. Chem.* **2015**, *87* (1), 230−249.



https://doi.org/10.1021/acsomega.5c01700
*ACS Omega* 2025, 10, 20713−20722